

Submillimetre observations of X-ray active galactic nuclei in the William Herschel Deep Field

R. M. Bielby,^{*} M. D. Hill, N. Metcalfe and T. Shanks

Department of Physics, Durham University, South Road, Durham DH1 3LE

Accepted 2011 September 8. Received 2011 September 5; in original form 2011 July 8

ABSTRACT

We investigate the contribution made by active galactic nuclei (AGN) to the high-redshift, luminous, submillimetre (submm) source population using deep (≤ 2 mJy beam⁻¹) Large Apex Bolometer Camera (LABOCA) 870 μ m observations within the William Herschel Deep Field. These submm data complement previously obtained *Chandra* X-ray data of the field, from which AGN have been identified with the aid of follow-up optical spectra. From the LABOCA data, we detect 11 submm sources (based on a detection threshold of 3.2σ) with estimated fluxes of $\gtrsim 3$ mJy beam⁻¹. Of the 11 identified submm sources, we find that two coincide with observed AGN and that, based on their hardness ratios, both of these AGN appear to be heavily obscured. We perform a stacking of the submm data around the AGN, which we group by estimated N_{H} column density, and find that only the obscured ($N_{\text{H}} > 10^{22}$ cm⁻²) AGN show significant associated submm emission. These observations support the previous findings of Page et al. and Hill & Shanks that obscured AGN preferentially show submm emission. Hill & Shanks have argued that, in this case, the contribution to the observed submm emission (and thus the submm background) from AGN heating of the dust in these sources may be higher than previously thought.

Key words: galaxies: high-redshift – quasars: general – submillimetre: galaxies – X-rays: galaxies.

1 INTRODUCTION

It is thought that the production of submillimetre (submm) emission in the luminous galaxy population observed at ≈ 850 μ m is predominantly driven by star formation (e.g. Smail et al. 2004; Alexander et al. 2005a; Pope et al. 2006). However, there is increasing observational evidence for a significant contribution from active galactic nuclei (AGN) to the heating of dust, and hence the production of submm emission, in these galaxies. Certainly some fraction of submm sources are observed to emit hard X-rays and there is still the possibility that the observed X-rays are reflected or scattered, which would mean they could have a significantly higher luminosity at 10–30 keV energies than expected.

Obscured AGN (i.e. with $N_{\text{H}} > 10^{22}$ cm⁻²) in particular appear to show high submm fluxes, as identified both from statistical techniques (Lutz et al. 2010; Hill & Shanks 2011b) and targeted submm observations of known quasi-stellar objects (QSOs; e.g. Coppin et al. 2008b; Martínez-Sansigre et al. 2009). Page et al. (2004) presented samples of obscured and unobscured QSOs and suggested that there may be a difference between these two classes in the submm, with the obscured sources showing higher submm

fluxes (see also Mainieri et al. 2005, for a fainter example of type 2 QSO). This is a crucial observation since it implies that the unified AGN model – where X-ray obscured QSOs are interpreted as being viewed at a different angle than unobscured QSOs – may be incomplete. Instead, X-ray obscured QSOs may represent an earlier stage in QSO evolution, where the black hole formed within a dusty starburst galaxy, as suggested by Page et al. (2004). This would account for an intrinsic difference between the submm properties of obscured and unobscured AGN.

Recently, Carrera et al. (2011) presented an analysis of a $z = 1.82$ QSO associated with submm emission and which is surrounded by an overdensity of submm galaxies (both QSOs and submm galaxies are strong tracers of large-scale structure; e.g. Smith & Heckman 1990; Ellingson, Yee & Green 1991; Austermann et al. 2009; Chapman et al. 2009; Bielby et al. 2010; Siemiginowska et al. 2010; Matsuda et al. 2011). Based on spectral energy distribution (SED) fitting, they conclude that the emission in the mid-infrared (MIR) range is dominated by reprocessed AGN emission, whilst the submm is dominated by a starburst contribution. A similar result was found for a $z \approx 4$ QSO by Coppin et al. (2009). However, Hill & Shanks (2011a) fit galaxy counts and colours using optically defined pure luminosity evolution models, where dust reradiates absorbed optical light into IR spectra composed of local galaxy templates, across the MIR bands from 3.6 to 8 μ m and up to a redshift of at

^{*}E-mail: rmbielby@gmail.com

least $z = 2.5$. They show that a significant contribution from AGN to the 250–870 μm SED would remove the need to invoke a top-heavy initial mass function for high-redshift starburst galaxies. It may therefore be that reprocessed emission from AGN could be more important than previously thought.

Interestingly, a significant AGN contribution to the submm population could have relevance for the origin of the hard X-ray (i.e. 10–30 keV) background. At softer energies (i.e. $\lesssim 10$ keV), much of the X-ray background (XRB) is resolved into sources, usually AGN (Shanks et al. 1991). At harder energies, therefore, the expectation is that heavily obscured AGN may form the background (e.g. Comastri et al. 1995; Gilli, Comastri & Hasinger 2007). However, the hard X-ray sources that have so far been identified by *Chandra* and *XMM* are skewed towards lower redshift, peaking at $z < 1$ and hence have somewhat lower luminosities, $L_X \approx 10^{42} - 10^{44}$ erg s $^{-1}$ (e.g. Alexander et al. 2003). Most studies conclude that the contributing sources so far detected only comprise < 25 per cent of the XRB (Krivonos et al. 2005; Worsley et al. 2005, 2006; Daddi et al. 2007; Hickox & Markevitch 2007). Should submm sources contain obscured AGN, this may go some way to explaining the missing XRB flux.

There is some evidence that different populations of high-redshift galaxies host obscured AGN. For example, Daddi et al. (2007) reported that a number of *BzK*-selected galaxies show a thermal, warm dust excess at 24 μm resulting from faint, hard X-ray sources. The suggestion is that these are obscured QSOs, but again these X-ray sources may be too faint to account for any more than 25 per cent of the background at 10–30 keV [whilst we note that Alexander et al. (2011) have recently reanalysed the Daddi et al. (2007) galaxy sample with deeper X-ray data and found a factor of $\gtrsim 10$ fewer obscured AGN than originally suggested by Daddi et al. (2007)]. In terms of submm galaxies, stacked X-ray spectra show a broad Fe $K\alpha$ line (Alexander et al. 2005a), whilst many of the optical spectra of submm galaxies show evidence for broad lines. Additionally, high ionization lines indicative of AGN activity have also been detected at far-IR wavelengths in *Herschel* Spectral and Photometric Imaging Receiver (SPIRE) Fourier Transform Spectrometer (FTS) observations of a $z \approx 3$ submm galaxy (Valtchanov et al. 2011). Finally, Buswell & Shanks (2001) suggested that the obscured QSOs might explain the bright, ≈ 5 mJy, submm number counts if the QSOs had a temperature of ≈ 30 K (see also Almaini, Lawrence & Boyle 1999) and this is at least consistent with the temperatures being reported for the SCUBA Half Degree Extragalactic Survey (SHADES) submm sources by Coppin et al. (2008b). Thus, it may be that submm galaxies account for a further fraction of the XRB at 10–30 keV.

We have undertaken a survey designed to measure 870 μm fluxes for a sample of known quasars with the aim of comparing the properties of obscured versus unobscured AGN. This has been performed in the William Herschel Deep Field (WHDF; Metcalfe, Fong & Shanks 1995; Metcalfe et al. 2001, 2006), which is especially suitable for this survey thanks to a significant sample of spectroscopically confirmed quasars within a small, easily observable area. This includes both unobscured and heavily obscured sources matched in redshift and luminosity (Vallb -Mumbru 2004). Although not capable of producing definitive results on their own, the observations we present here are a crucial step towards identifying the contribution of AGN to the production of the submm emission in submm sources and, thus, this population’s contribution to the submm and XRBs. This paper therefore presents the results from the submm survey, focusing on statistical analyses that complement the analyses in Hill & Shanks (2011b),

and which will form the basis for further multiwavelength treatment of this issue.

2 THE WILLIAM HERSCHEL DEEP FIELD

The WHDF is a $\approx 7 \times 7$ arcmin 2 area centred at $\approx 00^{\text{h}}20^{\text{m}} + 00^\circ$ (J2000) which has a wealth of multiwavelength data and has been extensively studied over the past 15 years (Metcalfe et al. 1995, 2001, 2006; McCracken et al. 2000a,b).

The field has ultradeep, ground-based optical *UBRIZ* imaging from the William Herschel Telescope in La Palma (reaching $B < 27.9$) as well as near-IR (NIR) *H* and *K* imaging from Calar Alto and the UK Infrared Telescope and deep, high-resolution *I*-band imaging from the *Hubble Space Telescope*’s Advanced Camera for Surveys.

In addition to this comprehensive optical/NIR coverage, the WHDF also has *Chandra* X-ray coverage, reaching a depth of $\approx 10^{-15}$ erg s $^{-1}$ cm $^{-2}$ over the whole area with a total integration time of ≈ 70 ksec. These observations were undertaken between 2000 November and 2001 January. 170 X-ray sources were detected at $\geq 2\sigma$ significance, of which 69 were at $\geq 3\sigma$ and 36 at $\geq 5\sigma$. Spectroscopic follow-up of some of these X-ray sources was subsequently performed and these observations are described by Vallb -Mumbru (2004) and in Section 5.1 below. Further spectroscopic data (of star-forming and passive galaxies, respectively) have also been presented by B hm & Ziegler (2007) and Fritz, B hm & Ziegler (2009).

The most recent additions to the WHDF data are (a) an 870 μm submm survey, which we undertook between 2008 and 2009 and which is described in this paper, and (b) radio observations at 8.4 GHz ($\lambda = 3.6$ cm) acquired with the Expanded Very Large Array (EVLA) in New Mexico in 2010. The reduction of these radio data is under way.

3 SUBMM OBSERVATIONS AND DATA REDUCTION

3.1 Observations

We have acquired 21 h of observations of the WHDF with the Large Apex Bolometer Camera (LABOCA; Siringo et al. 2009) on the 12 m Atacama Pathfinder Experiment (APEX) telescope (G sten et al. 2006). The LABOCA instrument comprises 295 semiconducting composite bolometers arranged in a series of concentric hexagons. LABOCA is sensitive to radiation in a passband centred at 870 μm , with a full width at half-maximum (FWHM) of ≈ 150 μm .

The LABOCA beam has a FWHM of 18.6 arcsec and the total field of view (FoV) of the detector is 11.4 arcmin. The WHDF covers a region of $\approx 7 \times 7$ arcmin 2 , as noted above, so this field fits well into the FoV of LABOCA. The LABOCA detectors do not form a contiguous array, however, so to achieve full sampling of the field we carried out our observations using a standard spiral raster map pattern. In this process, the centre of the array is moved in a spiral pattern and whilst being shifted laterally in a raster configuration, in order to fully sample the FoV.

Our observations were carried out in two separate observing runs,¹ the first on 2008 August 29–30 and the second on 2009

¹ European Southern Observatory programme IDs 081.A-0897(A) and 083.A-0707(A)

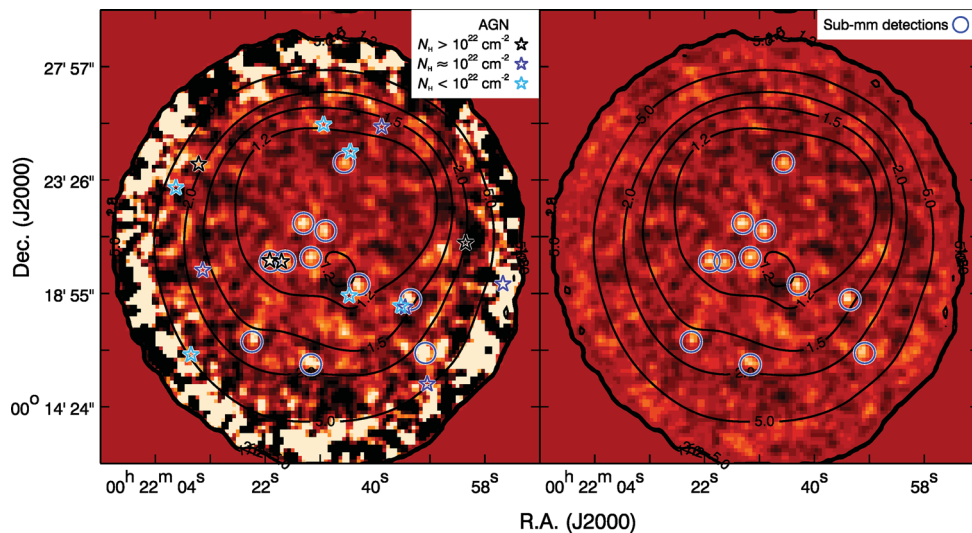


Figure 1. Left-hand panel: LABOCA 870 μm intensity map of the WHDF, with 11 sources detected at $\geq 3.2\sigma$ marked by open blue circles. The overlaid contours show the reduced noise map, with contour levels marked in mJy beam^{-1} . Spectroscopically identified QSOs (listed in Table 2) are also plotted, coded by their estimated hydrogen column density. The reduced off-axis sensitivity of LABOCA produces the increase in noise at the edges of the frame. Right-hand panel: LABOCA S/N map of the WHDF, with the same 11 sources marked. Again the contours show the reduced noise map.

May 11–12. The observing conditions were very good, with the range of zenith opacities, τ_z , spanning 0.17 to 0.23 in the first run and 0.17 to 0.28 in the second (these being calculated as standard from a linear combination of LABOCA 870 μm skydip results and opacities determined from the APEX radiometer).

3.2 Data reduction

Initial data reduction was performed using the standard BOA pipeline software (Schuller et al. 2010²) using the recommended sequence for ‘weak sources’. Counts from the detector are first converted into an output voltage, which can then be converted into a flux density, in standard units of Jy beam^{-1} , via a voltage–flux relation determined empirically during LABOCA’s commissioning. Sky removal was performed in BOA using the iterative medianNoiseRemoval command, which computes and corrects for the relative gains for a channel with respect to the mean signal. In addition to the usual despiking, data flagging, correlated noise removal and Fourier space filtering during the reduction, a DC offset (modelled by a first-order polynomial) is removed from each scan for each bolometer. A further correction is then applied to account for the zenith opacity at the time of observing. The zenith opacity, τ_z , is a measure of how much incoming radiation is absorbed by the atmosphere and is determined by ‘skydip’ observations (calibration exposures of the sky). Flux calibration was performed using observations of primary and secondary calibrators, with Uranus and Neptune being used as primary calibration sources during our observing run. The result of this process is a series of exposure maps for each scan of the target field. The maps were then co-added using BOA, which weights the signal from each scan image by $1/\sigma^2$, where σ is the pixel noise and is estimated by adding in quadrature the noise levels for each bolometer that contributes to a given pixel. The final output is a combined intensity (flux) map, as well as corresponding rms noise and signal-to-noise ratio (S/N) maps. Each of the maps has a pixel scale of $9.1 \text{ arcsec pixel}^{-1}$.

This data reduction process was carried out separately for the data from each of the two observing runs. As a final stage in the reduction process, therefore, we combined the maps, weighting them by the noise. The final intensity map was produced according to equation (1) and the final noise map according to equation (2):

$$I = \left(\frac{I_1}{\sigma_1^2} + \frac{I_2}{\sigma_2^2} \right) / \left(\frac{1}{\sigma_1^2} + \frac{1}{\sigma_2^2} \right), \quad (1)$$

$$\sigma = 1 / \sqrt{\frac{1}{\sigma_1^2} + \frac{1}{\sigma_2^2}}, \quad (2)$$

where I is intensity, σ is rms noise and subscripts 1 and 2 indicate the first and second observing runs. An S/N map was produced by taking the ratio of the two, and each of the maps was then Gaussian smoothed using the 18.6 arcsec beam profile, which gave a final resolution for the smoothed maps of 27 arcsec. The smoothing was comparable to that done by Weiß et al. (2009), who have shown that flux estimates from similarly smoothed maps are consistent with non-smoothed fluxes.

4 LABOCA DATA

The final intensity and S/N maps are shown in Fig. 1. It is clear from Fig. 1 that the noise increases substantially at large off-axis angles; in the S/N map (right-hand panel), this increase in the noise manifests itself as a dearth of sources around the edges of the frame. In the central 100 arcmin^2 area, the maps are very similar, with points of bright intensity having corresponding peaks in the S/N map, an indication that the noise level is relatively uniform across the field centre.

4.1 Noise level

Across the central 100 arcmin^2 region of the field, the data reach an rms noise level of $\lesssim 2 \text{ mJy beam}^{-1}$, making the WHDF one of the deepest submm fields observed to date (cf. fig. 6 of Weiß et al. 2009).

² www.mpifr-bonn.mpg.de/div/submmtech/software/boa/boaman.pdf

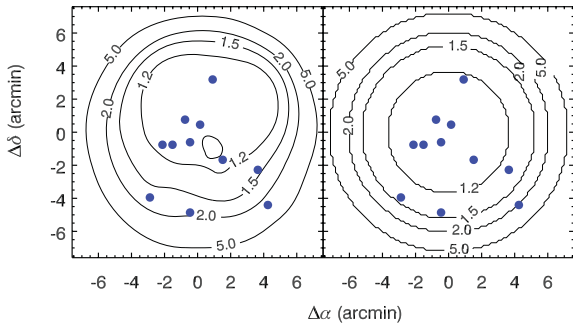


Figure 2. Noise contour maps of the WHDF, with the rms noise level marked at 1.2, 1.5, 2.0 and 5.0 mJy beam⁻¹, using (a) the pipeline-reduced noise map and (b) the standard deviation of the background flux measured in radial annuli. The image pixel size is 9.1 arcsec. 3.2 σ LABOCA sources are marked as blue circles. The maps generally agree well (see also Fig. 3). Most of our LABOCA sources are detected within the central region where the noise is lowest.

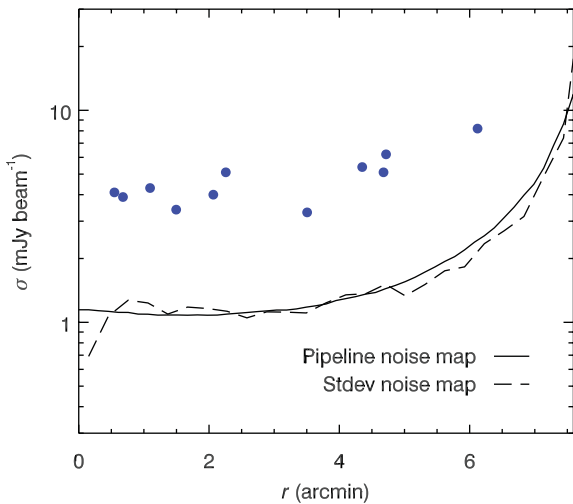


Figure 3. Radial noise profile of the WHDF showing the rms noise level, as a function of radius from the centre, for both the pipeline-reduced and standard deviation noise maps, described in the main text. 3.2 σ LABOCA sources are marked (blue circles) at their respective source flux and radial distance from the centre of the field.

To check the reliability of the pipeline-reduced noise map, we have produced a ‘standard deviation map’, by measuring the standard deviation of the intensity map in a series of annuli from the field centre, having masked out the bright sources (see Section 4.2). If the pipeline has worked successfully, this standard deviation map should be comparable to the BOA-produced noise map.

In Figs 2 and 3, we compare the contours and radial profiles, respectively, of the two maps. For the pipeline-reduced map, the noise profile shown in Fig. 3 is the median of 120 profiles measured radially at 3 arcmin intervals. The agreement between the two noise maps is very good – this is particularly clear from Fig. 3 – suggesting that the noise has been reliably estimated for our field and that our quoted depth of 2 mJy beam⁻¹ over an area of 100 arcmin² is robust.

4.2 LABOCA sources

The field contains 11 significant submm sources, circled in Fig. 1. We select the sources from the S/N map, with a criterion of

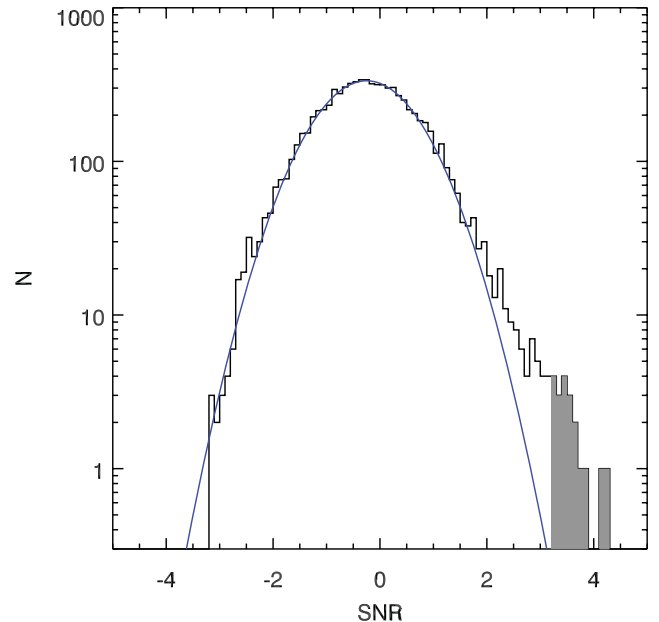


Figure 4. A histogram of pixel values from the S/N map. A Gaussian has been empirically fitted to the profile – most of the pixels lie within this distribution; however, a significant positive excess appears due to the presence of sources. The shaded region indicates those pixels lying above the 3.2 σ threshold we have set for source detection.

$S/N \geq 3.2$. This significance was chosen by comparing the map to its inverse: there are no negative spikes in the S/N map with a magnitude of 3.2 σ . This is illustrated in Fig. 4, which shows a pixel value histogram for the S/N map, with a Gaussian fit (blue curve). The map shows a strong positive excess, while the negative side of the distribution follows the Gaussian curve well. Based on the Gaussian fit, we estimate that the data would contain ≈ 0.2 spurious peaks above our chosen S/N limit within the central 100 arcmin² region.

The positions, S/N values and fluxes of the 11 sources are summarized in Table 1. We note that the quoted fluxes have not been corrected for the flux bias effect (Coppin et al. 2008a; Austermann et al. 2009); however, we do not consider this necessary for the scope of this paper. The positions of the 11 sources are indicated in Figs 1 and 2 and their fluxes are shown in comparison to the background noise in Fig. 3. Most of the sources lie within the < 2 mJy beam⁻¹ central area of the field, with 7/11 located within the $\sigma \leq 1.2$ mJy contour.

4.3 Completeness

We estimate the completeness of our submm observations using simulated sources placed in the final submm map across a range of fluxes. At each flux level, 500 sources are individually added to the map in turn and the detection analysis re-performed for each source. This is limited to the < 2 mJy beam⁻¹ region only and excluding regions within 2 pixel of any of the 11 detected sources. The result is shown by the filled black circles in Fig. 5, with the curve showing a polynomial fit to the result. Based on this analysis, we find the data to be 50 per cent complete at the 4.3 mJy beam⁻¹ level (shown by the dotted line).

Table 1. WHDF LABOCA 870 μm sources detected at $\geq 3.2\sigma$.

ID	RA (J2000)	Dec.	S/N	S_{870}^a (mJy beam $^{-1}$)	$\Delta\theta$ (arcsec)
WHDF-LAB-01	00:22:37.55	+00:19:16.8	4.3	5.1	9.4
WHDF-LAB-02	00:22:28.44	+00:21:42.6	4.2	4.3	9.6
WHDF-LAB-03	00:22:46.06	+00:18:40.3	3.8	5.4	10.7
WHDF-LAB-04	00:22:29.66	+00:20:20.5	3.7	4.1	10.9
WHDF-LAB-05	00:22:22.97	+00:20:11.4	3.6	4.0	11.3
WHDF-LAB-06	00:22:32.09	+00:21:24.3	3.6	3.9	11.3
WHDF-LAB-07	00:22:48.49	+00:16:32.8	3.5	8.2	11.6
WHDF-LAB-08	00:22:29.66	+00:16:05.4	3.4	6.2	11.9
WHDF-LAB-09	00:22:19.90	+00:17:00.1	3.2	5.1	12.7
WHDF-LAB-10	00:22:35.16	+00:24:08.3	3.2	3.3	12.7
WHDF-LAB-11	00:22:25.40	+00:20:11.4	3.2	3.4	12.7

^aWe note that listed fluxes are measured fluxes and not corrected for flux bias.

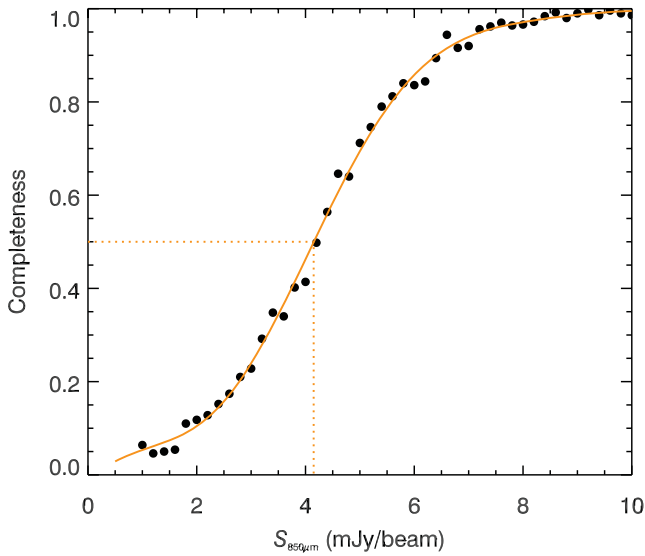


Figure 5. The completeness of the submm data ($< 2 \text{ mJy beam}^{-1}$ region only) estimated based on simulated sources placed in the submm image. The solid line shows a polynomial fit to the completeness estimates as a function of source brightness, with 50 per cent completeness marked by the dotted line at $S_{870 \mu\text{m}} = 4.2 \text{ mJy beam}^{-1}$.

5 SUBMM OBSERVATIONS OF WHDF QUASARS

5.1 Obscured and unobscured quasar samples

In Section 2, we briefly summarized the *Chandra* observations of the WHDF, which yielded detections of 170 X-ray sources. In 2001 and 2002, 36 of these WHDF X-ray sources were targeted in 10 h of spectroscopic follow-up with the Low Dispersion Survey Spectrograph 2 (LDSS2) multi-object spectrograph on the 6.5-m Magellan-1 (Walter Baade) telescope at the Las Campanas Observatory in Chile. These were optical observations, using a grism centred at $\lambda \approx 5500 \text{ \AA}$.

A stated aim of the LDSS2 observations was to investigate non-quasar X-ray sources, so the principal targets for spectroscopic follow-up were X-ray sources whose optical counterparts did not appear especially point-like (Vallb -Mumbru 2004). Nevertheless, 15 of the targets were spectroscopically confirmed as QSOs, and a

further two were classified as being either QSOs or narrow emission line galaxies. In this section, we take the 15 confirmed QSOs as our sample of WHDF quasars; details of these sources are given in Table 2.

The QSO classification was made by Vallb -Mumbru (2004) on the basis of both X-ray luminosity ($L_X > 10^{44} \text{ erg s}^{-1}$) and optical emission lines. Most of the sources classed as QSOs showed broad emission lines, including Ne v $\lambda 1240$, Si iv $\lambda 1400$, N iv $\lambda 1486$, He ii $\lambda 1640$, O iii] $\lambda 1663$ and/or N iii] $\lambda 1750$, all of which are AGN indicators. If broad lines were detected, the source was classified as a type 1 quasar, for example WHDFCH007 which is shown in the top panel of Fig. 6. One source was classified as a type 2 quasar on the basis of strongly detected narrow emission lines (WHDFCH008); its spectrum is shown in the bottom panel of Fig. 6.

The level of obscuration of an AGN can be estimated directly from the X-ray spectrum using the hardness ratio, HR. This is defined as $\text{HR} = (H - S)/(H + S)$, where H and S represent the photon counts in the hard (2–8 keV) and soft (0.5–2 keV) X-ray bands, respectively. Increasing levels of absorbing hydrogen column density produce greater absorption in the soft band than in the hard, so leading to larger values of HR. Assuming a given intrinsic spectral slope, Γ , the absorbing hydrogen column density can be estimated. Fig. 7 shows hardness ratio against redshift for our quasar sample, compared to the predicted tracks for quasars at different absorbing column densities (an intrinsic photon index of $\Gamma = 2$ is assumed).

The locus of the quasars is at $\text{HR} \approx -0.5$, consistent with the model that predicts $\text{HR} = -0.5$ for essentially all unobscured QSOs. Only four of the 15 QSOs are harder than $\text{HR} = -0.2$; these four sources – WHDFCH007, WHDFCH008, WHDFCH044 and WHDFCH099 – are expected to be highly obscured. WHDFCH007 and WHDFCH044 have extremely hard spectra with $\text{HR} \gtrsim 0.6$, corresponding to an apparent photon index of $\Gamma \approx -1$. Such sources are relatively rare, with for example only two $\text{HR} \approx 0.6$ objects being reported in the $\approx 2 \text{ deg}^2$ *XMM-Newton* cosmic evolution (COSMOS) survey (Mainieri et al. 2007; which we note is less deep by a factor of $\approx 2\text{--}3 \times$ than the WHDF X-ray data used here, whilst they do not present HR values with errors of > 0.3).

Based on Fig. 7, we divide the WHDF quasar sample into three groups: heavily obscured ($N_H > 10^{22} \text{ cm}^{-2}$), mildly obscured ($N_H \approx 10^{22} \text{ cm}^{-2}$) and unobscured ($N_H < 10^{22} \text{ cm}^{-2}$); these are marked in both Figs 1 and 7 by black, blue and cyan stars, respectively.

Table 2. Spectroscopically confirmed quasars in the WHDF. The positions, 0.5–10 keV fluxes (in $\text{erg s}^{-1} \text{cm}^{-2}$), X-ray hardness ratios and spectroscopic redshifts are given. Obscured quasars are indicated in bold.

ID ^a	RA (J2000)	Dec.	$S_{0.5-10}$ ($\text{erg cm}^{-2} \text{s}^{-1}$)	HR	z
WHDFCH005	00:22:35.963	00:18:50.04	5.62×10^{-14}	-0.60 ± 0.08	0.52
WHDFCH007	00:22:24.821	00:20:10.94	1.17×10^{-14}	$+0.82 \pm 0.33$	1.33
WHDFCH008	00:22:22.884	00:20:13.24	3.62×10^{-15}	-0.20 ± 0.24	2.12
WHDFCH016	00:22:45.164	00:18:22.64	1.44×10^{-14}	-0.43 ± 0.14	1.73
WHDFCH017	00:22:44.468	00:18:25.64	3.22×10^{-13}	-0.55 ± 0.03	0.40
WHDFCH020	00:22:36.142	00:24:33.84	1.09×10^{-14}	-0.55 ± 0.17	0.95
WHDFCH036	00:22:31.734	00:25:38.84	6.26×10^{-14}	-0.48 ± 0.06	0.83
WHDFCH044	00:22:55.092	00:20:55.74	2.66×10^{-14}	$+0.60 \pm 0.14$	0.79
WHDFCH048	00:22:41.297	00:25:33.34	2.15×10^{-14}	-0.43 ± 0.10	1.52
WHDFCH055	00:22:11.862	00:19:50.44	2.17×10^{-14}	-0.23 ± 0.06	0.74
WHDFCH090	00:22:48.795	00:15:18.74	4.83×10^{-14}	-0.41 ± 0.06	1.32
WHDFCH099	00:22:11.187	00:24:04.13	8.84×10^{-15}	$+0.11 \pm 0.18$	0.82
WHDFCH109	00:22:09.917	00:16:28.94	6.69×10^{-14}	-0.55 ± 0.08	0.57
WHDFCH110	00:22:07.433	00:23:07.74	2.20×10^{-14}	-0.43 ± 0.14	0.82
WHDFCH113	00:23:01.247	00:19:18.01	5.99×10^{-15}	-0.44 ± 0.45	2.55

^aAs in Vallbé-Mumbru (2004).

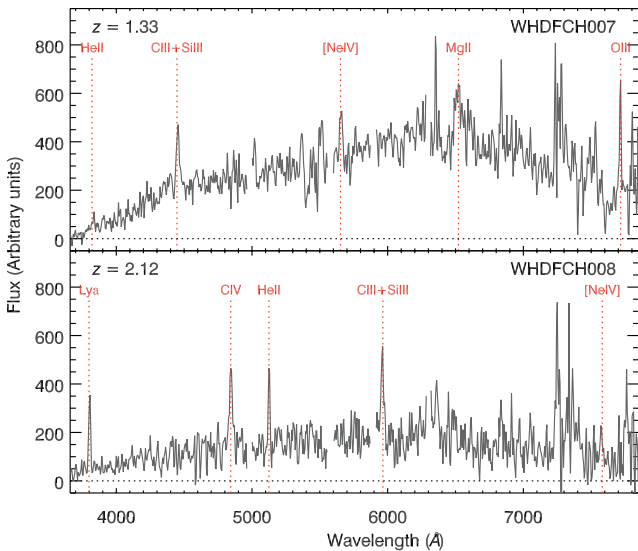


Figure 6. Optical spectra of WHDFCH007 (top) and WHDFCH008 (bottom) acquired with LDSS2 on the Magellan telescope. Both objects are associated with submm sources in our sample. Broad Mg II emission is observed in the spectrum of WHDFCH007. Only narrow emission lines are detected for WHDFCH008, which was classified as a type 2 QSO by Vallbé-Mumbru (2004).

5.2 Submm properties

5.2.1 Possible counterparts

We now look for associations between the submm sources found in the LABOCA data and the spectroscopically confirmed QSOs described above. For the purposes of this analysis, we restrict the sample to only those QSOs that lie within the 2 mJy beam^{-1} contours of the pipeline-reduced submm noise map shown in the left-hand panel of Fig. 2. This leaves two $N_{\text{H}} > 10^{22} \text{ cm}^{-2}$, three $N_{\text{H}} \approx 10^{22} \text{ cm}^{-2}$ and four $N_{\text{H}} < 10^{22} \text{ cm}^{-2}$ QSOs.

In order to identify coincident sources, we use a maximum separation between a QSO and a submm source of $2.5\Delta\theta$, where $\Delta\theta$ is the positional uncertainty on the given submm source

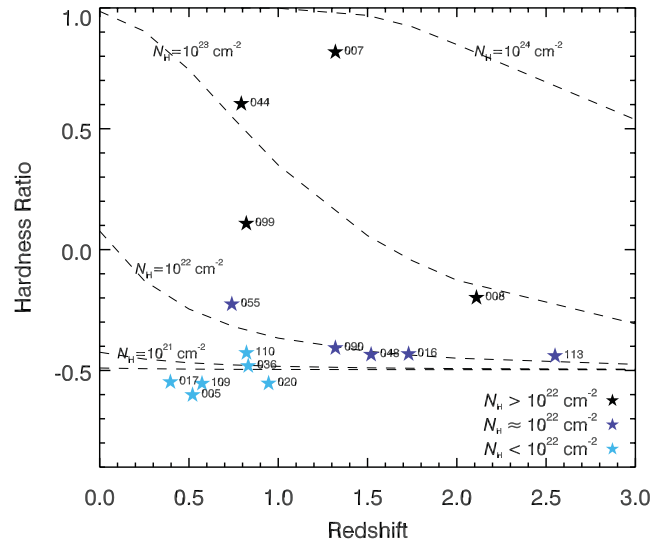


Figure 7. Hardness ratio versus redshift. The curves show predicted tracks for obscured QSOs at different column densities, which are indicated in the figure (in units of cm^{-2}). An intrinsic $\Gamma = 2$ power-law spectrum is assumed. Below $N_{\text{H}} = 10^{21} \text{ cm}^{-2}$ the lines become indistinguishable. WHDF X-ray QSOs are marked; each is labelled with its ID (with the WHDFCH prefix omitted). On the basis of this figure, we classify the QSOs into three categories: heavily obscured ($N_{\text{H}} > 10^{22} \text{ cm}^{-2}$; black), mildly obscured ($N_{\text{H}} \approx 10^{22} \text{ cm}^{-2}$; blue) and unobscured ($N_{\text{H}} < 10^{22} \text{ cm}^{-2}$; cyan).

(listed in Table 1). Given the S/N limit on our submm catalogue of $S/N = 3.2\sigma$, this gives a maximum possible separation of $2.5[0.6\theta(S/N)^{-1}] = 12.7 \text{ arcsec}$ (Ivison et al. 2007), with the smoothed map resolution of $\theta = 27 \text{ arcsec}$. The majority of the submm sources will have a separation constraint somewhat smaller than this however, given their higher S/N.

In order to evaluate the significance of a given alignment, we use the corrected Poisson probability, P , as employed by Downes et al. (1986). As such, we estimate the probability of a chance alignment using the observed integrated sky density of X-ray sources, $N(>S)$, as a function of the soft X-ray flux, $S_{0.5-2}$, which we calculate based on the power-law fit given by Vallbé-Mumbru (2004) for the WHDF

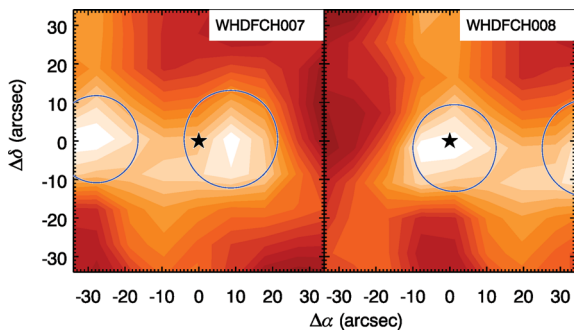


Figure 8. Thumbnail images of the LABOCA 870 μm intensity map at the positions of the highly obscured ($N_{\text{H}} > 10^{22} \text{ cm}^{-2}$) QSOs WHDFCH007 and WHDFCH008. In each case, the X-ray source position is marked by the star and nearby submm sources are marked by the blue circles (with the radii giving the estimated $2.5\Delta\theta$ positional accuracy). Both sources have closely associated submm emission.

sources:

$$\log N(>S_{0.5-2}) = -8.6 - 0.76 \log(S_{0.5-2}), \quad (3)$$

where $N(>S_{0.5-2})$ is in units of deg^{-2} and $S_{0.5-2}$ is in units of $\text{erg cm}^{-2} \text{ s}^{-1}$. We note that this is in good agreement with other such fits to the X-ray number counts (e.g. Mushotzky et al. 2000; Giacconi et al. 2001).

Based on the chosen $2.5\Delta\theta$ limits for identifying coincident sources, we find that two QSOs have possible LABOCA counterparts: WHDFCH007 (coincident with WHDF-LAB-11) and WHDFCH008 (coincident with WHDF-LAB-05). Fig. 8 shows thumbnail images of the LABOCA flux map at the positions of these X-ray sources, and $>3.2\sigma$ submm sources are seen close to the two QSOs. In each case, the star shows the location of the QSO and the blue circles show the $2.5\Delta\theta$ limit around nearby submm sources. The corrected Poisson probabilities that these are chance alignments are $P = 0.029$ and 0.004 (i.e. 2.9 and 0.4 per cent) for WHDFCH007 and WHDFCH008, respectively. For comparison, we note that Ivison et al. (2007) use a limit of $P \leq 0.05$ as a constraint for secure alignments between submm and $24 \mu\text{m}$ sources.

These two alignments are with QSOs in our highly obscured sample, whilst we note that the other two highly obscured quasars, WHDFCH044 and WHDFCH099, lie outside the imposed 2 mJy beam^{-1} noise limit. It is interesting, therefore, that of the two highly obscured WHDF QSOs which lie in the central, low-noise area of the field, both appear to have bright submm counterparts.

In Figs 9 and 10, we show thumbnail images for three $N_{\text{H}} \approx 10^{22} \text{ cm}^{-2}$ QSOs and four unobscured QSOs, respectively. Again we note that the full samples have six and eight sources, respectively, but those QSOs not shown are rejected due to lying outside the $<2 \text{ mJy beam}^{-1}$ noise region.

Some of the sources in these figures appear to lie close to bright areas, e.g. WHDFCH016 in Fig. 9 or WHDFCH017 in Fig. 10; however, none of these QSOs could be said to be *coincident* with a peak in the map as was the case for WHDFCH007 and WHDFCH008, lying as they do well outside the beam positional accuracy limits. We note that at the fluxes of the two submm sources associated with obscured AGN (i.e. $\approx 3\text{--}4 \text{ mJy beam}^{-1}$), our data are ≈ 30 per cent complete, which could compromise the observation that the $N_{\text{H}} \lesssim 10^{22} \text{ cm}^{-2}$ QSOs are not associated with submm emission to the level of the $N_{\text{H}} \gtrsim 10^{22} \text{ cm}^{-2}$ QSOs. In the following section, we therefore perform a stacking of each of the AGN populations to look for signatures of submm sources close to our detection threshold.

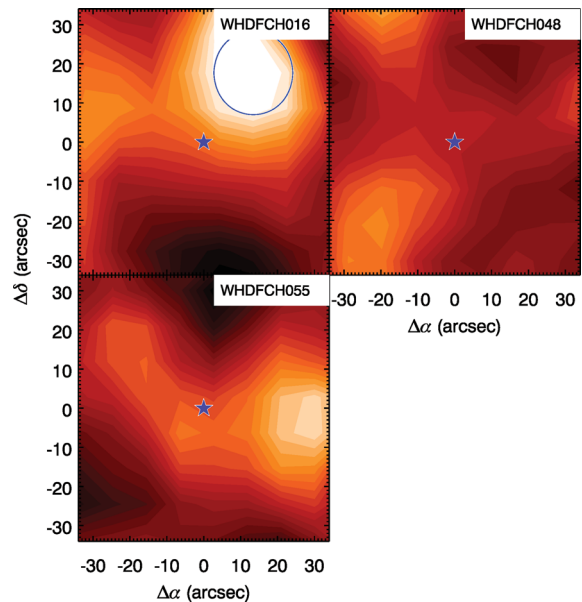


Figure 9. As in Fig. 8, but for sources characterized as mildly obscured with $N_{\text{H}} \approx 10^{22} \text{ cm}^{-2}$.

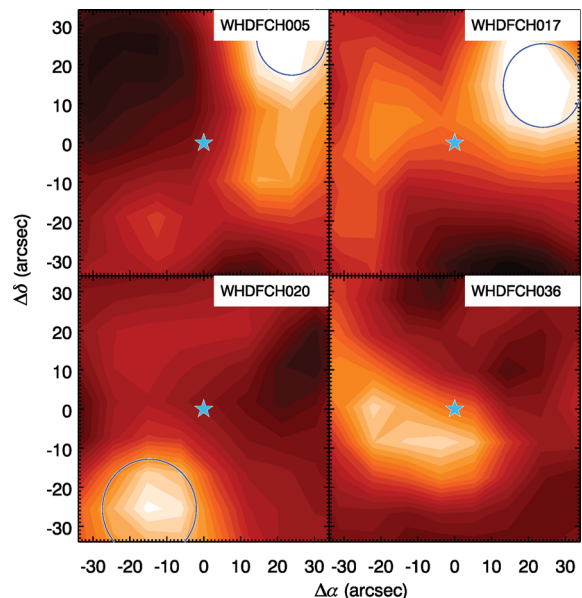


Figure 10. As in Fig. 8, but for sources characterized as unobscured with $N_{\text{H}} < 10^{22} \text{ cm}^{-2}$.

5.2.2 Stacking

To get an overall picture of the submm flux associated with our highly obscured, mildly obscured and unobscured quasar populations, we stack the submm flux maps for each of the populations. To ensure that the noisy fringe sources do not dominate the stacked flux, there are two ways to proceed – either to exclude the sources near the edge and stack only the sources linearly within the $<2 \text{ mJy beam}^{-1}$ region (exploiting the relatively uniform noise across the centre) or to perform a noise-weighted stack which mitigates the effect of the noisy objects. Having performed both analyses, we find the results are not significantly affected by the choice of method. In the analysis presented here, for simplicity we use stacks incorporating only

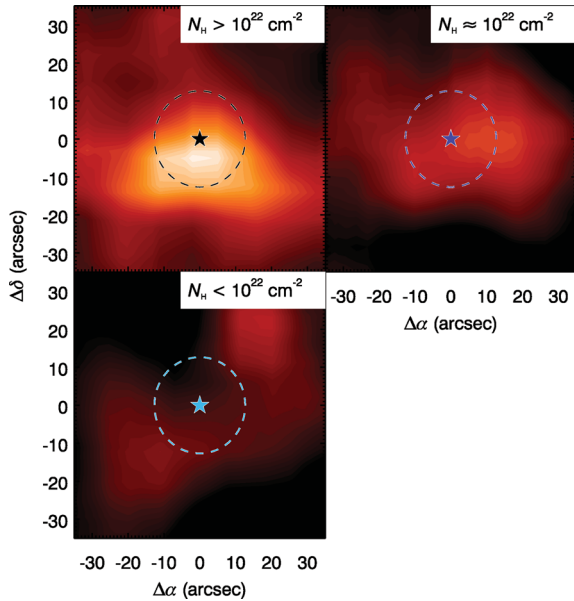


Figure 11. Noise-weighted stacked intensity maps for the three populations with $N_{\text{H}} > 10^{22} \text{ cm}^{-2}$, $N_{\text{H}} \approx 10^{22} \text{ cm}^{-2}$ and $N_{\text{H}} < 10^{22} \text{ cm}^{-2}$. The dashed circle in each case shows the maximum search radius of $\Delta\theta = 12.7$ arcsec used in matching the QSOs and submm sources. Only the most highly obscured QSOs show significant stacked submm emission.

those sources within the $< 2 \text{ mJy beam}^{-1}$ region, without any noise weighting.

The stacked flux images for the three QSO populations are shown in Fig. 11, incorporating two sources in the $N_{\text{H}} > 10^{22} \text{ cm}^{-2}$ sample, three sources in the $N_{\text{H}} \approx 10^{22} \text{ cm}^{-2}$ sample and four sources in the $N_{\text{H}} < 10^{22} \text{ cm}^{-2}$ sample. Taking the peak value within our maximum search radius of 12.7 arcsec, we find a peak signal of $S_{870 \mu\text{m}} = 3.4 \pm 0.8 \text{ mJy beam}^{-1}$ at an angular distance of 5 arcsec from the QSO positions for the $N_{\text{H}} > 10^{22} \text{ cm}^{-2}$ stack. For the $N_{\text{H}} \approx 10^{22} \text{ cm}^{-2}$ and $N_{\text{H}} < 10^{22} \text{ cm}^{-2}$ stacks, we find peak signals of $S_{870 \mu\text{m}} = 1.9 \pm 0.8$ and $0.7 \pm 0.5 \text{ mJy beam}^{-1}$, respectively (both being found at an angular distance of ≈ 10 arcsec from the stack centre). These plots reinforce the observations based on individual X-ray sources that the highly obscured quasars are the only sources to be associated with submm bright sources, without being affected by the completeness of the submm data at the $\approx 3\text{--}4 \text{ mJy beam}^{-1}$ flux level.

5.2.3 Statistical power

It is important to account for the statistical power afforded by the small numbers of objects involved in the current analysis. We therefore estimate the confidence limits of the sample size presented here (based on the tabulated small sample Poisson statistics provided by Gehrels 1986) for the fraction of unobscured and obscured AGN associated with submm emission. Based on the sample of two obscured AGN, we estimate that our observations give a lower limit of 35 per cent on the percentage of such objects having associated $\gtrsim 3 \text{ mJy beam}^{-1}$ submm emission (at the 1σ level). Conversely, the sample of $N_{\text{H}} < 10^{22} \text{ cm}^{-2}$ gives an upper limit of 37 per cent on the percentage of these unobscured AGN being associated with $\gtrsim 3 \text{ mJy beam}^{-1}$ submm emission (again at the 1σ level). Although the samples considered here are small and cannot fully constrain the relationship between AGN obscuration and submm emission, our analysis remains consistent with a model in which submm emission arises preferentially from more obscured AGN – in agreement with

the analyses of, for example, Page et al. (2004), Lutz et al. (2010) and Hill & Shanks (2011b).

5.3 Future improvements

Despite the relatively poor resolution of our submm data, it appears that each of the X-ray QSOs WHDFCH007 and WHDFCH008 has only a small chance of accidentally aligning with a submm source. It is notable that only the most obscured AGN show possible $870 \mu\text{m}$ detections and these include the type 2 QSO, WHDFCH008. Stacking the submm data as a function of X-ray absorption also provides further evidence that faint, X-ray obscured QSOs are preferentially submm bright.

Further tests of the reality of the associations between the two X-ray obscured QSOs and the LABOCA sources will soon be available from the 8.4 GHz EVLA radio survey of the WHDF, which will have $\approx 2 \times$ improved spatial resolution compared to the LABOCA data. These data are still at the reduction stage and the results will be reported in a later paper.³

In addition, we are seeking *Herschel* observations at 250, 350 and 500 μm , which will constrain the SED and allow dust temperatures to be measured for the detected sources. If the unobscured QSOs are found to be detected in these shorter wavelength bands, it could reveal whether any temperature difference exists between obscured and unobscured quasars, as was hypothesized by Hill & Shanks (2011b).

Finally, we are also proposing to observe the two X-ray obscured QSOs with Atacama Large Millimetre/submillimetre Array (ALMA) in its extended configuration to investigate further the submm counterparts of these sources. Not only will ALMA give better positional information but its ≈ 0.5 arcsec angular resolution will allow us to test if the associated submm sources are point-like or extended at $\lesssim 3 \text{ kpc}$ spatial resolution.

6 CONCLUSIONS

We have presented an $870 \mu\text{m}$ survey of the well-studied WHDF, reaching a depth of $< 2 \text{ mJy beam}^{-1}$ over an area of 100 arcmin^2 . In total, 11 sources have been detected at a significance of $\geq 3.2\sigma$. From the noise distribution of the image, we estimate the number of false detections in the 100 arcmin^2 region to be ≈ 0.2 , whilst the completeness in the same region is 50 per cent at a flux of $4.3 \text{ mJy beam}^{-1}$.

We find that two of the 11 submm sources are likely counterparts of X-ray-selected WHDF quasars: WHDFCH007, an extremely hard QSO with $\Gamma \approx -1$, and WHDFCH008, a type 2 QSO with only narrow optical emission lines, both consistent with being heavily obscured. We divide a sample of 15 WHDF quasars into three subsets, having $N_{\text{H}} < 10^{22}$, $N_{\text{H}} \approx 10^{22}$ and $N_{\text{H}} > 10^{22} \text{ cm}^{-2}$, and find that only the most obscured population shows any significant stacked $870 \mu\text{m}$ flux.

Although based on a relatively small sample, our findings are supportive of a model in which obscured AGN are submm bright and unobscured AGN are not. This picture of faint X-ray obscured AGN being preferentially stronger submm emitters is difficult to fit into the unified AGN model without some adaptation, given that both X-ray obscured and unobscured AGN would be expected to be equally strong submm emitters in this case. Nevertheless, the observational results of, for example, Page et al. (2004), Alexander et al. (2005a), Lutz et al. (2010), Hill & Shanks (2011b) and now

³ We note that since submission of this paper, both WHDFCH007 and WHDFCH008 have been detected in the 8.4 GHz EVLA data.

the results presented here in the WHDF all tend to support the idea that obscured AGN are more frequently submm emitters than unobscured AGN.

From these results, two solutions have been proposed: either (a) AGN heating is a dominant component of dust heating, producing submm emission (e.g. Granato & Danese 1994; Willott et al. 2002; Grimes, Rawlings & Willott 2005; Hill & Shanks 2011b), or (b) obscured AGN are an evolutionary concurrent phenomenon with strong star formation and it is the star formation that is the dominant mechanism for the dust heating in these objects (e.g. Page et al. 2004; Alexander et al. 2005b; Vignali et al. 2009; Lutz et al. 2010).

Assuming the former, Hill & Shanks (2011b) argue that the contribution of obscured AGN to the submm background may be as much as ≈ 40 per cent (compared to ≈ 13 per cent in the unified/evolutionary model case). In addition, the same authors suggest that, should the primary driver of submm emission in these sources be heating from obscured AGN, then these may be the source of a significant fraction of the $\gtrsim 10$ keV XRB, whilst the contribution would be much lower should heating from star formation be the dominant mechanism. Other potential candidates still fall short of fully accounting for the XRB (e.g. Worsley et al. 2005; Gilli, Comastri & Hasinger 2007; Treister, Urry & Virani 2009) and, in this context, quantifying the contribution from obscured AGN in the submm source population is an important goal. Although we are unable to inform fully on this based on the results here, these observations remain an important step in the process.

Upcoming radio data, as well as proposed observations in the submm and other bands, will enable further investigation of the submm properties of obscured and unobscured AGN in the WHDF. As discussed, *Herschel* observations will add important constraints to the SEDs of these objects and facilitate the measurement of dust temperatures, whilst the obscured QSOs will also make excellent targets for high-resolution observations with ALMA. Crucially, such observations would not only improve on the accuracy of the submm source positions, but would also inform on whether the submm sources are extended, indicating a galaxy-wide starburst origin, or point-like and therefore more associated with the activity in the nucleus.

ACKNOWLEDGMENTS

We would like to thank J. Geach for assistance in reducing the submm data presented here and R. Hickox for comments on the text. MDH acknowledges the support of an STFC PhD Studentship grant, whilst RMB, NM and TS acknowledge the support of STFC funding. We also thank the anonymous referee for his/her contribution. This publication is based on data acquired with the Atacama Pathfinder Experiment (APEX). APEX is a collaboration between the Max-Planck-Institut für Radioastronomie, the European Southern Observatory and the Onsala Space Observatory.

REFERENCES

Alexander D. M. et al., 2003, *AJ*, 126, 539
 Alexander D. M., Bauer F. E., Chapman S. C., Smail I., Blain A. W., Brandt W. N., Ivison R. J., 2005a, *ApJ*, 632, 736
 Alexander D. M., Smail I., Bauer F. E., Chapman S. C., Blain A. W., Brandt W. N., Ivison R. J., 2005b, *Nat*, 434, 738
 Alexander D. M. et al., 2011, *ApJ*, 738, 44
 Almaini O., Lawrence A., Boyle B. J., 1999, *MNRAS*, 305, L59
 Austermann J. E. et al., 2009, *MNRAS*, 393, 1573
 Bielby R. M. et al., 2010, *A&A*, 523, A66
 Böhm A., Ziegler B. L., 2007, *ApJ*, 668, 846

Busswell G. S., Shanks T., 2001, *MNRAS*, 323, 67
 Carrera F. J., Page M. J., Stevens J. A., Ivison R. J., Dwelly T., Ebrero J., Falocco S., 2011, *MNRAS*, 413, 2791
 Chapman S. C., Blain A., Ibatova R., Ivison R. J., Smail I., Morrison G., 2009, *ApJ*, 691, 560
 Comastri A., Setti G., Zamorani G., Hasinger G., 1995, *A&A*, 296, 1
 Coppin K. et al., 2008a, *MNRAS*, 384, 1597
 Coppin K. E. K. et al., 2008b, *MNRAS*, 389, 45
 Coppin K. E. K. et al., 2009, *MNRAS*, 395, 1905
 Daddi E. et al., 2007, *ApJ*, 670, 173
 Downes A. J. B., Peacock J. A., Savage A., Carrie D. R., 1986, *MNRAS*, 218, 31
 Ellingson E., Yee H. K. C., Green R. F., 1991, *ApJ*, 371, 49
 Fritz A., Böhm A., Ziegler B. L., 2009, *MNRAS*, 393, 1467
 Gehrels N., 1986, *ApJ*, 303, 336
 Giacconi R. et al., 2001, *ApJ*, 551, 624
 Gilli R., Comastri A., Hasinger G., 2007, *A&A*, 463, 79
 Granato G. L., Danese L., 1994, *MNRAS*, 268, 235
 Grimes J. A., Rawlings S., Willott C. J., 2005, *MNRAS*, 359, 1345
 Güsten R., Nyman L., Schilke P., Menten K., Cesarsky C., Booth R., 2006, *A&A*, 454, L13
 Hickox R. C., Markevitch M., 2007, *ApJ*, 661, L117
 Hill M. D., Shanks T., 2011a, *MNRAS*, 414, 1875
 Hill M. D., Shanks T., 2011b, *MNRAS*, 410, 762
 Ivison R. J. et al., 2007, *MNRAS*, 380, 199
 Krivonos R., Vikhlinin A., Churazov E., Lutovinov A., Molkov S., Sunyaev R., 2005, *ApJ*, 625, 89
 Lutz D. et al., 2010, *ApJ*, 712, 1287
 McCracken H. J., Metcalfe N., Shanks T., Campos A., Gardner J. P., Fong R., 2000a, *MNRAS*, 311, 707
 McCracken H. J., Shanks T., Metcalfe N., Fong R., Campos A., 2000b, *MNRAS*, 318, 913
 Mainieri V. et al., 2005, *MNRAS*, 356, 1571
 Mainieri V. et al., 2007, *ApJS*, 172, 368
 Martínez-Sansigre A. et al., 2009, *ApJ*, 706, 184
 Matsuda Y. et al., 2011, *MNRAS*, 416, 2041
 Metcalfe N., Fong R., Shanks T., 1995, *MNRAS*, 274, 769
 Metcalfe N., Shanks T., Campos A., McCracken H. J., Fong R., 2001, *MNRAS*, 323, 795
 Metcalfe N., Shanks T., Weibacher P. M., McCracken H. J., Fong R., Thompson D., 2006, *MNRAS*, 370, 1257
 Mushotzky R. F., Cowie L. L., Barger A. J., Arnaud K. A., 2000, *Nat*, 404, 459
 Page M. J., Stevens J. A., Ivison R. J., Carrera F. J., 2004, *ApJ*, 611, L85
 Pope A. et al., 2006, *MNRAS*, 370, 1185
 Schuller F., Nord M., Vlahakis C., Albrecht M., Beelen A., Bertoldi F., Mueller S., Schaaf R., 2010, *BoA User Manual*. <http://www.mpifr-bonn.mpg.de/div/submmtech/software/boa/boaman.pdf>
 Shanks T., Georgantopoulos I., Stewart G. C., Pounds K. A., Boyle B. J., Griffiths R. E., 1991, *Nat*, 353, 315
 Siemiginowska A., Burke D. J., Aldcroft T. L., Worrall D. M., Allen S., Bechtold J., Clarke T., Cheung C. C., 2010, *ApJ*, 722, 102
 Siringo G. et al., 2009, *A&A*, 497, 945
 Smail I., Chapman S. C., Blain A. W., Ivison R. J., 2004, *ApJ*, 616, 71
 Smith E. P., Heckman T. M., 1990, *ApJ*, 348, 38
 Treister E., Urry C. M., Virani S., 2009, *ApJ*, 696, 110
 Vallb -Mumbru M., 2004, PhD thesis, Durham Univ.
 Valtchanov I. et al., 2011, *MNRAS*, 415, 3473
 Vignali C. et al., 2009, *MNRAS*, 395, 2189
 Weiß A. et al., 2009, *ApJ*, 707, 1201
 Willott C. J., Rawlings S., Archibald E. N., Dunlop J. S., 2002, *MNRAS*, 331, 435
 Worsley M. A. et al., 2005, *MNRAS*, 357, 1281
 Worsley M. A., Fabian A. C., Bauer F. E., Alexander D. M., Brandt W. N., Lehmer B. D., 2006, *MNRAS*, 368, 1735

This paper has been typeset from a $\text{\TeX}/\text{\LaTeX}$ file prepared by the author.